J MATER RES TECHNOL. 2020;9(1):857–867

Available online at www.sciencedirect.com

jmr&t Journal of Materials Research and Technology

www.jmrt.com.br

Original Article

Fabrication and characterizations of Al nanoparticles doped ZnO nanostructures-based integrated electrochemical biosensor

K. Gherab[a], Y. Al-Douri[b,c,d,*], U. Hashim[a], M. Ameri[e], A. Bouhemadou[f], Khalid Mujasam Batoo[g,**], Syed Farooq Adil[h], Mujeeb Khan[h], Emad H. Raslan[i]

[a] Instituteof Nano Electronic Engineering, University Malaysia Perlis, 01000 Kangar, Perlis, Malaysia
[b] University Research Center, Cihan University Sulaimaniya, 46002, Iraq
[c] Nanotechnology and Catalysis Research Center (NANOCAT), University of Malaya, 50603 Kuala Lumpur, Malaysia
[d] Department of Mechatronics Engineering, Faculty of Engineering and Natural Sciences, Bahcesehir University, 34349 Besiktas, Istanbul, Turkey
[e] Laboratoire Physico-Chimie des Matériaux Avancés (LPCMA), Université Djilali Liabès de Sidi Bel-Abbès, Sidi Bel-Abbès, 22000, Algeria
[f] Laboratory for Developing New Materials and Their Characterization, University of Setif 1, 19000 Setif, Algeria
[g] King Abdullah Institute for Nanotechnology, King Saud University, P.O. Box 2455, Riyadh, 11451, Saudi Arabia
[h] Department of Chemistry, College of Science, King Saud University, P.O. Box 2455, Riyadh 11451, Saudi Arabia
[i] Department of Physics, College of Science, King Saud University, P.O. Box 2455, Riyadh 11451, Saudi Arabia

ARTICLE INFO

Article history:
Received 5 April 2019
Accepted 11 November 2019
Available online 21 November 2019

PACS:
75.75.Fk
77.55.hf
87.85.fk
88.10.gp

Keywords:
AZO
Sol–gel method
Characterization
Optical

ABSTRACT

The benefits of the electrical-based biosensor include cheap production and fast response time of detecting diseases. An interdigitated electrode (IDE) is fabricated using silver (Ag) as a metal contact that is deposited on aliminium (Al) nanoparticles doped with both zinc oxide (ZnO) and Silicon (Si) forming AZO/Si nanostructures by vacuum coater in a thermal evaporator. The electrical properties are studied as a function of frequency and voltage using I–V characteristics. Sol–gel method under annealing temperature, 500 °C is utilized to generate Al nanoparticles doped ZnO nanostructures. UV–vis spectrophotometer, Atomic Force Microscopy (AFM), Scanning Electron Microscopy (SEM) and X-ray diffractometer (XRD) are used for analyzing optical, topographical, morphological and structural studies of AZO nanostructure, respectively. Specific empirical models of optical dielectric constant, bulk modulus and refractive index are also verified.

© 2019 The Authors. Published by Elsevier B.V. This is an open access article under the CC BY-NC-ND license (http://creativecommons.org/licenses/by-nc-nd/4.0/).

* *Corresponding author at*: Nanotechnology and Catalysis Research Center (NANOCAT), University of Malaya, 50603 Kuala Lumpur, Malaysia.
** *Corresponding author*.
E-mails: yarub@um.edu.my, yarub.aldouri@sulicihan.edu.krd (Y. Al-Douri), kbatoo@ksu.edu.sa (K.M. Batoo).
https://doi.org/10.1016/j.jmrt.2019.11.025
2238-7854/© 2019 The Authors. Published by Elsevier B.V. This is an open access article under the CC BY-NC-ND license (http://creativecommons.org/licenses/by-nc-nd/4.0/).

1. Introduction

Different applications in detecting diseases, growth of cells and bacteria, toxins and monitoring of disease progression may potentially benefit from biosensor devices [1]. Electrochemical biosensors represent an important subclass of chemical sensors, where an electrode is used as transduction element [2]. They are inexpensive, suitable for designing integrated microsystems and rapid response [3]. The resistive characteristics of materials and analysis of capacitive (or inductive) in response to the small amplitude of sinusoidal excitation signal are combined by electrochemical impedance [4]. The mechanism of impedance detection is based on the measurement of impedance change as a result of binding of target molecules to receptors (proteins, antibodies, DNA and other bio-recognition elements) adhered onto electrodes' surfaces [5–7]. Biosensors are attractive and successfully used in several applications like medical diagnosis [8], clinical chemistry [9], environmental fields [10], infection diagnosis [11], food industry [12] and DNA damage [13].

Different fields of technology and science are applying interdigitated electrode (IDE) to function as actuators and/or transducers with particular emphases in the areas of chemical sensors [14], biological sensing [15], biosensors [16] and gas sensing [17] that are utilized as label-free based biosensor for detection of molecules onto surface of electrodes. Various techniques have been reported to manufacture and apply IDE electrochemical biosensor. Sanguino et al. [18] have reported the deposited ZnO nanorod structures on micrometer interdigitated Au electrodes as three-dimensional matrices for immobilization of antibodies in a capacitive immunosensors format. Moreover, Azizah et al. [19] have introduced a high-performance sensing method by using IDEs to spatially arranged DNA immobilization on 10-nm gold nanoparticles (GNP) deposited on silicon substrate. Siddiquee et al. [20] have utilized ZnO nanoparticles and ionic liquid on gold electrode for constructing of electrochemical biosensors to detect DNA hybridization by using cyclic voltammetry under optimal conditions. Furthermore, Haarindraprasad et al. [21] have fabricated ZnO nanowire based IDE to detect the level of blood glucose. IDE is manufactured with Ag using wet etching-assisted conventional lithography, the gap between adjacent electrodes is 98.80 mm. The process of printing a comb electrode structure in a reliable manner required extreme care and design [22]. Separate electrodes shapes such as multi-islands of IDEs, planer IDEs, 3-D micromesh electrodes, ring array electrodes and octagonal interdigitated ring electrodes [23] are utilized.

Several interdigitated finger electrodes make up the IDE, in which the IDEs are usually constructed from materials of noble metal such as Ag [24], Pd [25], C [26], Pt [27], Au [28]. CuO nanosheets (NSs) electrode [29] and indium-tin-oxide (ITO) [30]. Among these metals, electrode based on silver is being studied intensively and attracting commercial interest owing to its great potential for flexible, large-scale fabrication and cost-effective [31]. Previous research has shown that silver provides excellent conductivity and extensibility for using in this work [32]. Besides, in biosensors Ag facilitate more efficient electron transfer than other metals like gold [33].

A pure and Al- and/or Ca-added ZnO fibers were synthesized by Santangelo et al. [34] via electro-spinning method. They have reported that all fibers are made up of rounded polycrystalline oxide nanoparticles that are linked to each other, with the surface roughness controlled by the (dopant-dependent) nanoparticle size. The samples and their photoluminescence characteristics are strongly affected by non-stoichiometry. Meanwhile, Norek et al. [35] have generated ZnO nanorods onto the anodic aluminum oxide (AAO) templates via Atomic Layer Deposition (ALD) method. Two versions of samples are created with distinct arrangements of ZnO nanorods and doping conditions. Nanorods are co-doped with Al, in order to stimulate defect-related emissions. The interior of AAO nanopores is heterogeneously filled with ZnO materials, which has a hexagonal quartzite structure. Yun et al. [36] have investigated the dye-sensitized solar cells (DSSCs)'s performance based on Al-doped and undoped ZnO nanorod arrays, which are generated via a simple hydrothermal approach. When Al-doped ZnO nanorod arrays are grown in 0.04 M zinc acetate dihydrate solution with 5 mM aluminum nitrate monohydrate, the maximum energy conversion efficiency (η) reached is 1.34% in DSSC. This result has displayed a great increase of η in Al-doped ZnO nanorod-based DSSCs as compared to undoped 0.05%. Lastly, Cobalt doped ZnO nanomaterial (CZN) was successfully generated by Yang and Nie [37] with Co content from 2 to 10 mol% through a novel freeze-drying method. The CZN's band gap from ultraviolet-visible (UV–vis) spectroscopy reduces as Co doping increases. It is called the n-type semiconductor material [38]. Several applications have benefited from ZnO, which includes optoelectronics, sensors, biological devices [39], organic light emitting diodes, solar cells [40] photocatalysis, ultraviolet lasers [41], cancer treatment, photodetectors and piezoelectric devices [42]. Sol–gel method is one of the simplest mechanism used to improve the production of ZnO nanostructure [43]. Sol–gel enables powderless processing of nanostructured thin films and fibers directly from solution. By a mixing procedure at molecular level, materials of various shape may be formed at much lower temperatures than it is made possible by traditional methods of preparation [44,45]. On the other hand, most sol–gel processes start from a solution containing source compounds for the target material; the solution becomes a sol as a result of the formation of fine colloidal particles or polymers and further reactions lead to gelation, which is the wet gel formation in the course of sol-to-gel conversion. Whereby, spin coating, fiber drawing and molding into bulky shapes can be done [46].

ZnO has been reported to deposit by many ways including thermal evaporation, pulse laser deposition, spray pyrolysis [47] and metal organic chemical vapor deposition (MOCVD) [48]. Hence, the spin-coating technique has attraction due to its simplicity and low cost [49]. In the current study, a series of effective, simple and successful stages permit the fabrication of IDE biosensor devices onto AZO nanostructure. The AZO nanostructure is prepared and then deposited onto p-silicon substrate at annealing temperature, 500 °C via spin-coating technique. Furthermore, the AZO nanostructure's structural, morphological and optical characteristics are studied by utilizing UV–vis spectrometer,

Atomic Force Microscopy (AFM), Scanning Electron Microscopy (SEM) and X-ray diffractometer (XRD), respectively. Elaboration of IDE's design and fabrication, as well as detailed description of experimental steps, are made. Moreover, I–V measurements have characterized their electrical properties.

2. Materials and methods

2.1. Synthesis of ZnO solution

Sol–gel method is utilized to prepare the ZnO solution via a successful and simple chemical route, using monoethanolamine ($(HOCH_2CH_2)$ NH2) (MEA), 2-methoxyethanol (CH_3O $(CH2)_2OH$) (2-ME) and zinc acetate $(CH_3COO)_2$ Zn as a sol stabilizer, solvent and solute, respectively. The zinc acetate powder has a concentration, 0.2 mol/L (200 mg), which is dissolved in 20 ml of 2-methoxythanol in a beaker on a hot plate with a magnetic stirrer (WiseStir MSH 30D) at 1000 rpm rotated speed for 30 min at 60 °C. The MEA is added slowly under constant stirring of ten minutes for two hours at 80 °C. The molar ratio of zinc acetate to MEA is adjusted as 1:1. A more homogenous and clear solution is developed by keeping the resultant solution at room temperature for one hour.

2.2. Al NPs doped ZnO nanostructure

It is reported that the required electrical and optical characteristics to achieve maximum transparency in ZnO can be obtained by heavily doping with distinct dopants including Al [50]. Al NPs sized 70 nm is blended with distilled water and stirred at 80 °C for 2 h. Therefore, the solution is homogeneous and maintained at room temperature for 48 h. Subsequently, ZnO is doped by 3 at % of Al NPs and maintained for the next stage.

2.3. Wafer preparation

In order to remove all outstanding impurities, the p-Si, <100> is prepared in ultrasonic cleaner (DELTA DC200H, Taiwan) by submerging in RCA1 solutions. Additionally, p-Si of <100> is polished in one side, with diameter of 100 mm and thickness of 525 mm. The silicon wafer is then cleaved into 15 pieces with size of 2×2 cm.

2.4. ZnO nanostructure coating procedure

For the purpose of depositing the solution on the substrate, spin-coater (Laurell WS-400B, USA) is utilized at a speed of 2500 rpm for 20 s and 500 rpm for 10 s. Then, the dip-coated AZO/Si assembly is dried at a pre-heat temperature of 100 °C for one minute in order to get a uniform nanostructure layer with a suitable thickness as displayed in Fig. 1. Lastly, a diffusion furnace (MODU6LAB, USA) is utilized to apply annealing temperature on the sample at 500 °C for a duration of 1 h, under the steady flow of nitrogen gas (N_2), in order to maintain the coherence of deposited nanostructures.

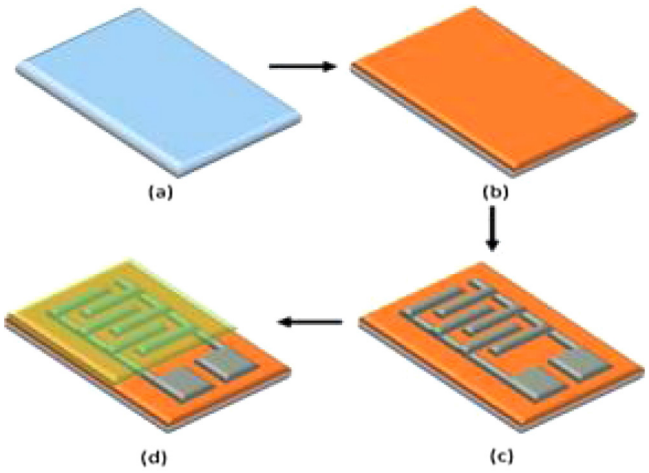

Fig. 1 – Schematic illustration of IDEs fabrication steps (a) Si substrate, (b) Si / AZO, (c) Si /AZO/ IDE, (d) Si /AZO / IDE (Ag).

2.5. Interdigitated electrode (IDE) fabrication

There are various benefits offered by the IDE, Fig. 1d, such as quick reaction kinetics, increased signal to noise ratio and swift set up of steady-state. IDE is manufactured with Ag/p-Si (Fig. 1a) and AZO (Fig. 1b) substrates by vacuum coater of thermal evaporator. The grown electrodes have thickness of 100 nm. A cross section of the three layers IDE Ag/AZO/Si is shown in Fig. 1.

2.6. Analysis and characterization of AZO nanostructure

UV–vis spectrophotometer (Perkin Elmer Lambda 35, USA) is utilized to investigate the reflection at wavelength range, 200–1000 nm. X-ray diffractometer at Bragg's angle (2θ), 20–60° at 4°/min rate is used to explore the structural characteristics. AFM (SPA 400, Seiko Instruments Inc, USA) including surface of $5 \times 5\,\mu m$, rate of 1 Hz and SEM (SEM JSM-6010LV, USA) is employed for examining morphology and topography. Furthermore, (Alpha-A High-Performance Modular Measurement System, novo control, USA) and (KEITHLEY 6487, Tektronix, USA) are applied to characterize IDEs' electrical characteristics.

3. Results and discussion

3.1. Optical properties

As shown of Fig. 2a, UV–vis spectroscopy in the range, 200–1000 nm is utilized to perform reflection measurements at room temperature, in order to get the reflectance spectrum of nanostructured AZO, 3 at.% grown on p-Si substrate at 500 °C. It is observed that reflection rises with rising annealing temperature, up to the highest reflectance of 84% at 500 °C. Tauc equation is used to estimate the value of band gap for AZO nanostructure's and presented in Table 1 [51]:

$$(\alpha h\nu)^2 = A\,(h\upsilon - E_g) \quad (1)$$

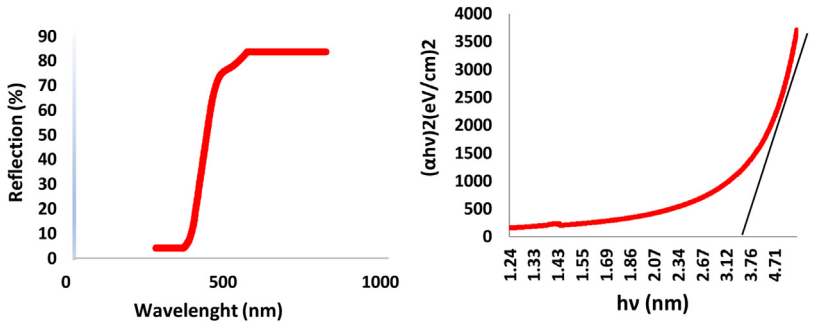

Fig. 2 – (a) Reflectance spectrum and (b) plot of $(\alpha h\upsilon)^2$ vs photon energy $h\upsilon$ of AZO nanostructure deposited on p-Si substrate at 500 °C.

Table 1 – The structural parameters of AZO nanostructure by XRD and energy gap corresponding to refractive index and optical dielectric constant.

2θ	Particle size (D) (nm)	Full width at half maximum (FWHM)	Miller indices (hkl)	Interplaner distances (d) (Å)	Lattice constants (a and c) (Å)	B_0 (GPa)	Strain (ε)	Dislocation density (δ) (10^{14}lines/m^2)
34.22	13.79	0.6298	002	2.61994	a = 3.02, c = 5.33	90.61	0.026	5.25

No. crystallites particles/area (N) ($\times 10^{15}$)	Thick. (t) (nm)	Crystallite size (nm)	Rough. (nm)	Thick. (nm)	Eg (eV)	n	ε_∞
0.2020	529.80	94.88	1.97	529.80	3.67	1.77[a] 2.16[b] 2.24[c]	3.13[a] 4.66[b] 5.01[c]

[a] Ref. [54].
[b] Ref. [55].
[c] Ref. [56].

in which energy band gap is represented by E_g, the photon energy is presented by $h\upsilon$, absorption coefficient = 0.023/d × ln 1/T is represented by α and A refers to a constant [52]. The plots between $h\upsilon$ and $(\alpha h\upsilon)^2$ are depicted in Fig. 2b. As shown in this figure, the E_g is calculated by extrapolating the linear portion to the photon energy axis. Fig. 2b illustrates that E_g rises with rising annealing temperature to higher energy band gap, 3.61 eV at 500 °C, which is considerably greater than bulk ZnO, 3.37 eV. The material's band gap is associated with electron's excitation from the top of valence band to bottom of conduction band. The rising carrier density causes the rising of Fermi level into conduction band of degenerate semiconductor.

This resulted in broadening the band gap as photons incident energy has bigger energy gap at visible region and absorbed by ZnO. It also provides less noise and bigger stability for AZO based devices. Non-radiative crystal defects are reduced at annealing temperature of 500 °C, in addition to enhance optical absorbance. Furthermore, at annealing temperature of 500 °C, the grain size increases and produces a final single crystal AZO nanostructure, which is highly sought crystal structure utilized in electro-biosensor. This result indicates that AZO nanostructure's surface under annealing temperature, 500 °C has great structural and optical characteristics due to great energy value. This illustrates an improvement in the ability to develop optoelectronics.

An important physical parameter in microscopic atomic interactions is the refractive index (n). In theory this index is associated with these entities' density and local polarizability [53]. There are attempts to investigate many simple relationships between energy gap (E_g) and refractive index (n) [54–61]. In order to validate the current work, various links between E_g and n have been reviewed. A linear relationship displays high-frequency refractive index, while band gap is suggested by Ravindra et al. [54]:

$$n = \alpha + \beta E_g \tag{2}$$

where $\alpha = 4.048$ and $\beta = -0.62\ eV^{-1}$.

Taking inspiration from the simple physics of light dispersion and refraction, the following empirical relation is proposed by Herve and Vandamme [55]:

$$n = \sqrt{1 + \left(\frac{A}{E_g + B}\right)^2} \tag{3}$$

in which $A = 13.6$ eV and B=3.4 eV.

A distinct method is taken by Ghosh et al. [56] to consider the concept of Penn [62] and Van Vechten [63] for quantum-dielectric formulations and band structure. The following expression is developed using B, which is a constant added to the lowest band gap E_g and A is a contribution from the valence electrons,

$$n^2 - 1 = A/(E_g + B)^2 \tag{4}$$

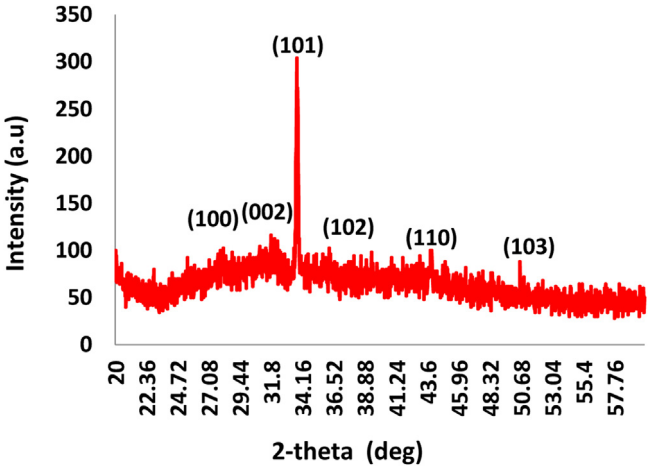

Fig. 3 – XRD pattern of AZO nanostructure deposited on p-Si at 500 °C.

in which $A = 25E_g + 212$, $B = 0.21E_g + 4.25$ and $(E_g + B)$ refers to a suitable average energy space of material. Thus, there are attempts by these three models for variation of n with E_g. Furthermore, the equation $\varepsilon_\infty = n^2$ is utilized to calculate the optical dielectric constant (ε_∞) [64]. Table 1 lists the estimated optical dielectric constant and refractive index. It proves that Ravindra et al. [54] model is a suitable for applications.

3.2. *Structural properties*

As shown of Fig. 3, the AZO nanostructure's XRD is grown on p-Si substrate by sol–gel method at 500 °C. XRD pattern has displayed in low 2θ at 40 kV and 30 mA for optimized and extended conditions from 20 to 60° at 0.04○, scanned speed per second. There are six major diffraction peaks for AZO nanostructure deposited at room temperature, appearing at $2\theta = 50.60$, 43.86, 35.72, 33.60, 31.80 and 28.16°, which are attributed to (103), (110), (102), (101), (002), and (100), respectively at 500 °C. It reaffirms the single phase, hexagonal quartzite structure of doped and pure ZnO sample. Table 1 presents the lattice parameters (a and c) of the prepared samples. Calculations are made using Bragg's Law [65]:

$$n\lambda = 2dSin\theta \tag{5}$$

where n is diffraction order, λ is wavelength of X-ray, hkl are Miller indices and d is space between planes. The following equation gives an estimation of the interplanar spacing (d) [66]:

$$\frac{1}{d^2} = \frac{4}{3}\frac{h^2 + hk + k^2}{a^2} + \frac{l^2}{c^2} \tag{6}$$

The lattices constants (a) and (c) obtained from [67]:

$$a = \frac{\lambda}{\sqrt{3}Sin\theta} \tag{7}$$

$$c = \frac{\lambda}{Sin\theta} \tag{8}$$

Based on the Debye-Scherrer's formula, the size of average crystallite size can be deduced from full-width at half maximum (FWHM) of highest XRD peak [68]:

$$D = \frac{\lambda k}{FWHM * cos\theta} \tag{9}$$

in which D refers to the crystallite size, shape factor equals 0.9 for hexagonal lattice is referred to k, the wavelength is represented by $\lambda = 0.15406$ nm for CuKα source, and Bragg angle is represented by θ. The measured results are depicted in Fig. 4 and displayed in Table 1, based on Scherrer's formula.

Table 1 displays the dislocation density (δ) and strain (ε), which are derived from the following formula [69]:

$$\delta = 1/D^2 \tag{10}$$

$$\varepsilon = \frac{\beta cos\theta}{4} \tag{11}$$

Moreover, the number of crystallites particles (N) is as follows [70]:

$$N = \frac{t}{D^3} \tag{12}$$

where t refers to thickness.

Measurement of material stiffness is termed bulk modulus. Investigation of solid's thermodynamic properties has been done by distinct groups [71–78]. Thermodynamic characteristics such as inter-atomic separation and bulk modulus of solids with featured best-fit relations and approximations

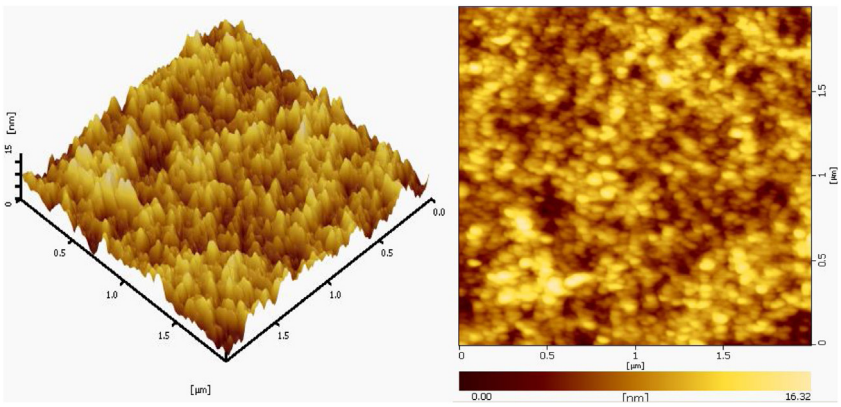

Fig. 4 – 3-D and 2-D of AFM images of AZO nanostructure deposited on p-Si at 500 °C.

have been investigated by our group [73,72–76]. Computation of electronic and structural characteristics are possible to be performed. A lot of time and effort are required for *ab initio* calculations. Thus, there has been development of empirical methods to compute material characteristics. There is an applicability benefit to a wide class of materials offered by empirical approach. Despite not being able to provide highly accurate results, these empirical methods are still beneficial in terms of application. An empirical formula is established by Cohen [79] for calculating bulk modulus B_0 followed by nearest-neighbor distance. The author results are in accordance with experimental data. An analytical expression of bulk modulus from total energy was developed by Lam et al. [80]. A same numerical result is generated, in which they found an analytical expression for the pressure derivative of B_0. An empirical formula for B_0 is proposed by our group using the lattice constant's concept. Results are collected in line with theoretical and experimental ones. It is essential to proceed with experimental conditions and hypothetical structure in order to fully utilize this formula for future applications.

Lattice constant may be linked to bulk modulus, with major influence being the covalency degree characterized by Phillips' homopolar gap E_h [77]. A stimulus to present this information is the verification of our calculation that is not restricted to compute space. As such, we trust that this data will be useful for future investigations. The clear distinction between lattice constants for AZOs, as observed in Table 1 is to provide an incentive to investigate B_0. The lattice constants as presented in Table 1 are the basis of our model. The following empirical formula is provided by fitting these data [81]:

$$B_0 = [3000 - 100\lambda]\left(\frac{a}{2}\right)^{-3.5} \quad (13)$$

where a is lattice constant (Å), while the empirical parameters, which accounts for the influence of ionicity is represented by λ: with $\lambda = 2$, 1, 0 for group II–VI, III–V, and IV semiconductors, respectively. The Al NPs influence the attribution of nanostructure and cause AZOs' bulk modulus to have a specific value. The results show that the calculated bulk modulus gives similar chemical trends derived from literature.

3.3. *Topographical and morphological studies*

The AZO nanostructure deposited on p-Si has illustrated topography at 500 °C. The 2-D and 3-D AFM images with 1 Hz scan rate and 5×5 μm area are shown in Fig. 4. Grain size, roughness and thickness as given in Table 1 are 94.88, 1.97 and 529.80 nm, respectively. The bigger surface and sensitivity have less nanostructured roughness for multi-application.

To notice a roughness decreasing accompanied by increased AZO nanostructure, the degree of surface roughness decreases due to increment of AZO grain-size. This result proves that AZO nanostructure's topography at 500 °C is providing a highly crystalline, uniform and impactful property. These benefits contribute to its utilization as a device in bio sensing-related applications.

The AZO nanostructure deposited on p-Si shows morphology at 500 °C as depicted in Fig. 5. As displayed, there is a shape alteration of seeded layer and enhanced grain

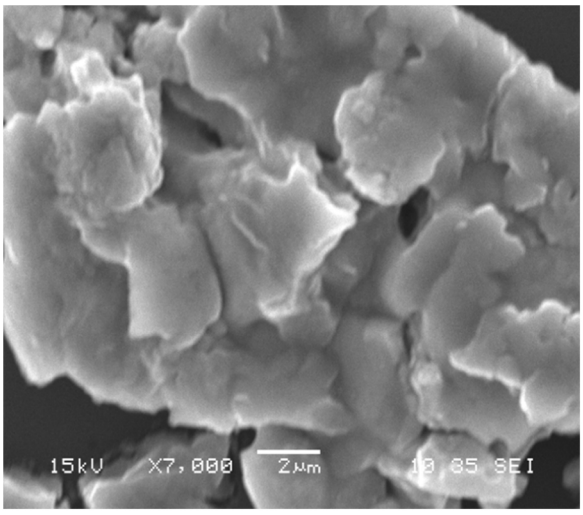

Fig. 5 – SEM image of AZO nanostructure deposited on p-Si substrate at 500 °C.

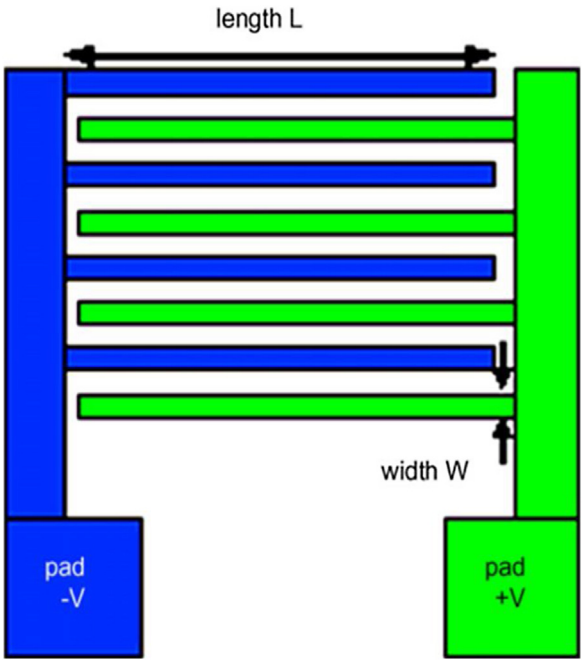

Fig. 6 – IDE structure with multiple non-contact fingers.

size as a result of the involvement of Al doping ZnO nanostructure and the present baking-annealing steps at 500 °C. It demonstrates a good size, complete coverage, minimum defect and better homogeneity. The grain particles' arrangement is strongly influenced by surface uniformity of AZO nanostructure in which the surface uniformity is highly influenced by grain particle as a result of grain coordination.

3.4. *Electrical properties*

The p-Si wafer is utilized as a base of IDE device. IDEs are fabricated by utilizing Ag and deposited onto AZO/Si substrate

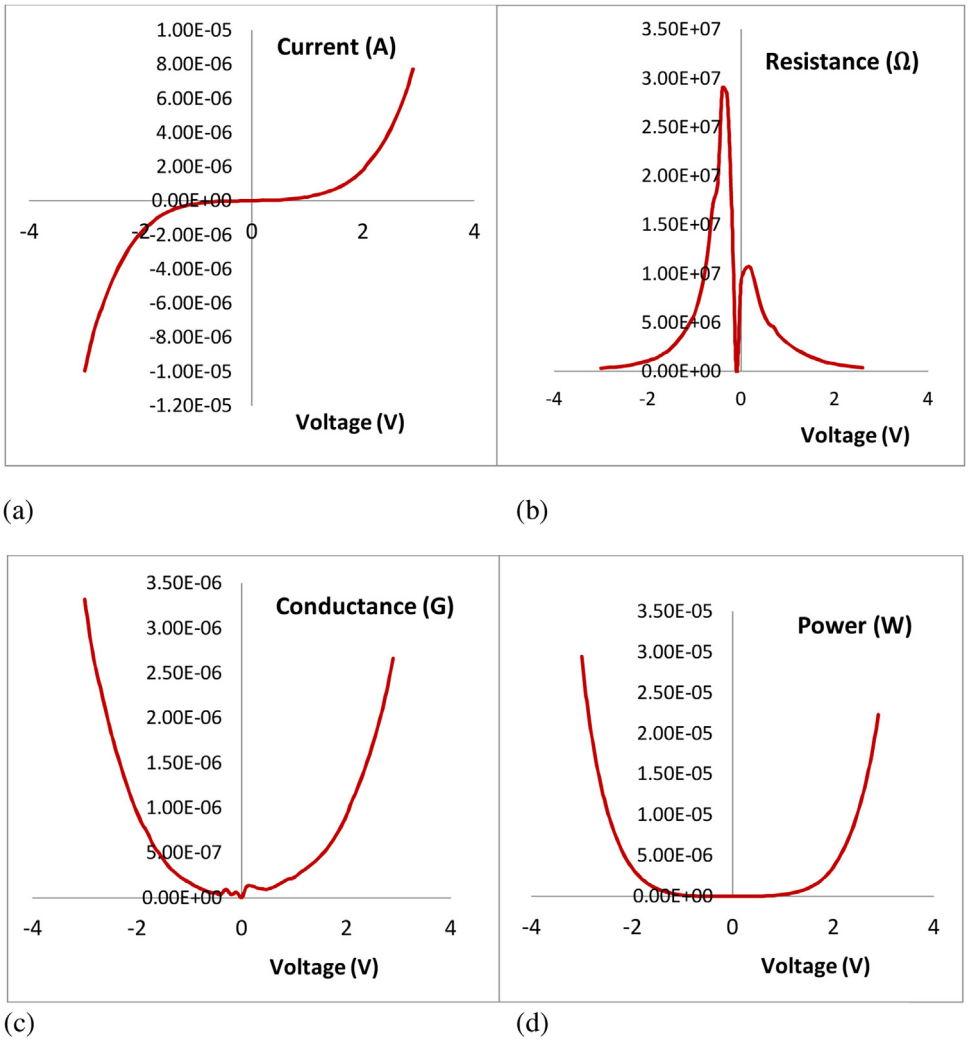

Fig. 7 – Electrical characteristics of IDEs using KEITHLEY 6487 as a function of (a) current versus voltage (I–V), (b) resistance versus voltage, (c) conductance versus voltage, and (d) power versus voltage.

by thermal evaporator as shown in Fig. 1. The design of IDE is up to 4 pairs of finger electrodes with dimension, 0.25 mm gap (G) between 2 adjacent IDEs, 3.75 mm long (L) and 0.25 mm wide (W). In addition, the wavelength (λ) is 1 mm while the fingers' thickness is 100 nm. The structure of IDE is illustrated in Fig. 6.

3.4.1. *I–V measurement using Keithley*

As shown in Fig. 7, KEITHLEY 6487 is utilized to measure I–V properties of AZO nanostructure. The sheet resistance is projected by measuring the reverse linear fit of I–V plots [49] including applied voltage scale from 3 to −3 V. I–V curves show the finite value of current at 0 V, while IDEs possess metallic electrodes on AZO/Si. The resulted current via the device rose from -10×10^{-3} to 10×10^{-3} nA with semi-linear behavior identified as Schottky barrier as shown in Fig. 7a. The barrier is generated in a junction of metal-semiconductor (MS). IDE has an electrode on AZO/Si substrate. The resistance (R) is a ratio of voltage (V) to current (I).

$$R = V/I \tag{14}$$

As shown in Fig. 7b, the resistance initiates at −3 V from 0.306 MΩ and increases until −0.6 V, where resistance works up to 30 MΩ then decreases to 10 MΩ, subsequently it fluctuates between −0.6 and −0.3 V. It is noticed that high resistance scale is between −0.3 to −1.1 V. The huge gap between two adjacent IDEs leads to high resistance. The conductance indicates the ability of electricity to stream under a particular path, while the inverse is denoted by resistance (R)

$$G = \frac{I}{V} = \frac{1}{R} \tag{15}$$

$$R = V/I \tag{16}$$

This is described in Fig. 7c and can see that conductance behavior is the same as resistance behavior, without fluctuation. However, it is in the opposite direction. Input voltage times current is noted in Watts as referred by the electrical power (P).

$$P = VI \tag{17}$$

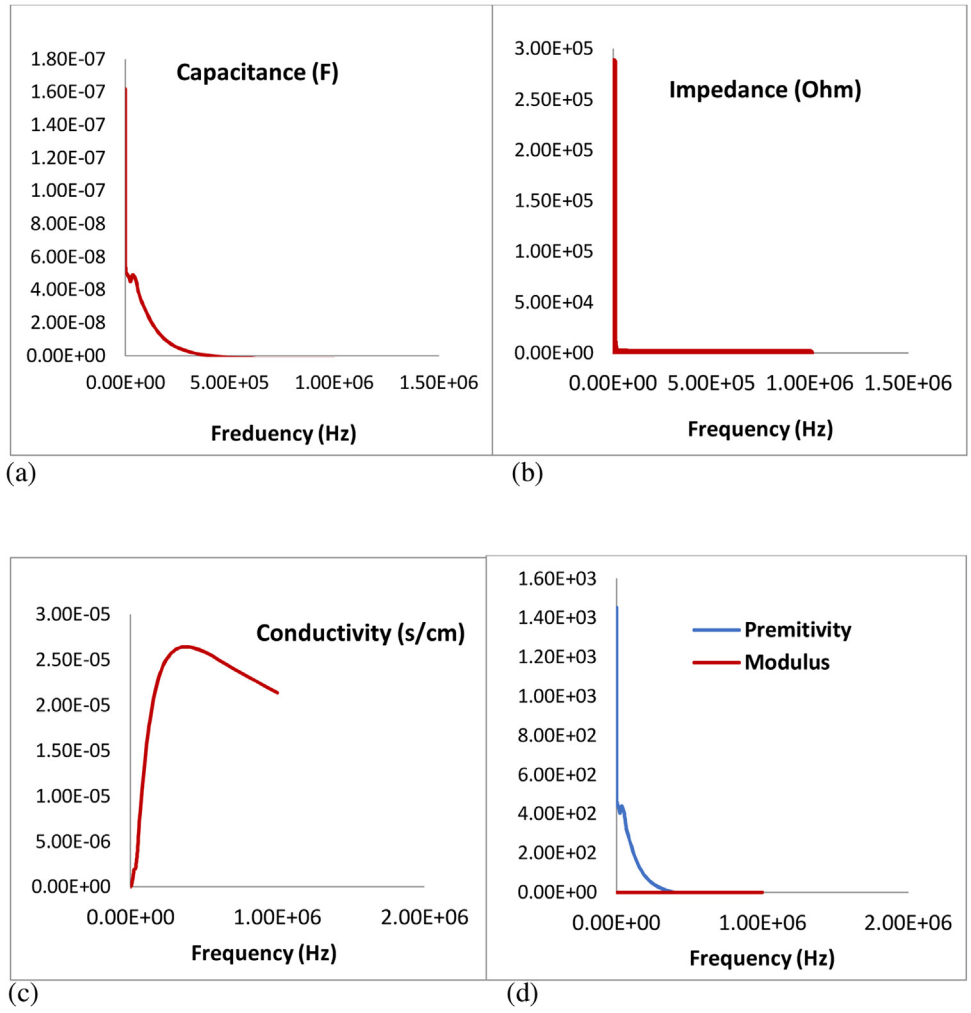

Fig. 8 – Electrical characteristics of IDEs using Alpha-A analyzer as a function of (a) capacitance versus frequency (I–V), (b) impedance versus frequency, (c) conductivity versus frequency, and (d) permittivity and modulus versus frequency.

As shown in Fig. 7d, the power curve is noted to be a concave, starting from 30,000 nW at −3 V and continued to drop to 0 W at 0 V, followed by rising power to 23,000 nW at 3 V.

3.4.2. *I–V measurement using alpha-analyzer*

In order to discover a distinguished parameter of electricity in terms of frequency and voltage, Alpha-A is employed to implement the second set of measurements. The resulted capacitance can be tested in terms of capacitor of parallel plate that is linked in the following:

$$C = \varepsilon A/d \tag{18}$$

where d is the separation distance between fingers, A is contact area and ε is dielectric constant. It is possible to improve the variation of capacitance if a short space is available between electrodes. The IDEs capacitance in terms of frequency is shown in Fig. 8a. A reverse relationship between frequency and capacitance is available, in which the capacitance initiates from 0.65 nF at 1 MGz and continues to rise with reducing frequency up to 162 nF at 1 Hz. Electrical impedance refers to measurement of non-faradic that arises from the interface polarization or capacitance, and is gained from the following empirical formula:

$$Zc = \frac{1}{j\omega C} \tag{19}$$

where j is an imaginary section, $w = 2\pi f$ refers to omega possesses unit of radian per second, while C is the capacitor. The IDEs' impedance is shown in Fig. 8b in terms of frequency, where it is noticed that a reversed relationship occurs between impedance and frequency. The impedance starts at 1 MHz from 37 Ω with reduced frequency to 2400 KΩ at 1 Hz. The reciprocal quantity of resistivity is referred to as electrical conductivity. The measurement of degree of electrical conduction by a material is termed as conductivity.

$$\sigma = \frac{1}{\rho} \tag{20}$$

where ρ is the electrical resistivity as:

$$\rho = \frac{RA}{l} \tag{21}$$

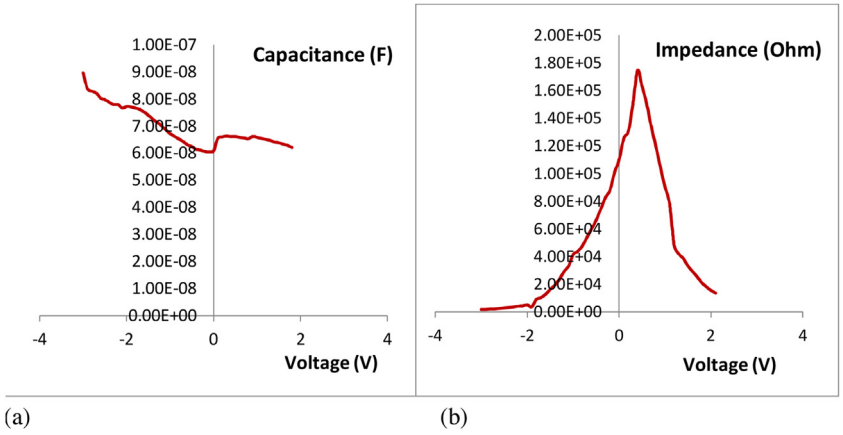

Fig. 9 – Electrical characteristics of IDEs using Alpha-A analyzer as a function of (a) capacitance versus voltage (I–V) and (b) impedance versus voltage.

where R is the material's electrical resistance, l is the material's length and A is material's cross-sectional area. Fig. 8c describes conductivity of IDEs in terms of frequency, where a reduction occurs at 1 MHz from 26,400 nS/m to 3.32 nS/m at 1 Hz. The reverse electric modulus is dipected as complex relative permittivity (ε). IDEs' modulus and permittivity are illustrated in Fig. 8d in terms of frequency. It is noticed that permittivity initiates with −10 F/m at 1 MHz and increases with reduced frequency until 1450 F/m at 1 Hz. Contrarily, the electric modulus starts at 1 MHz with −9980 m/F then decreases with reduced frequency until −3850 m/F at 1 Hz. To explore impedance and capacitance in terms of voltage, another set of measurement is done by utilizing Alpha-A. The IDEs' capacitance is shown in Fig. 9a as a function of voltage in which w is fairly stable. It is initiated from 8.96 nF at −3 V and continue to experience fluctuations until it reaches 6.21 nF at 3 V. There are other evolutions in Fig. 9b, with the impedance initiating from 1.63 KΩ at −3 V and continuing to rise exponentially, where the highest value is 175 KΩ at 0.4 V, then decreases to 13.6 KΩ at 3 V.

4. Summary and conclusions

Sol–gel method at 500 °C was utilized to synthesize and deposit AZO nanostructure on p-Si substrate. In order to get an excellent crystalline structure with sharp and intense peak, it was optimized at distinct parameters. The XRD results showed that the energy band gap was 3.67 eV as demonstrated by UV–vis. In addition, the topographical and morphological studies have shown greater homogeneous AZO nanostructures. Ravindra et al. model have proved to be suitable for AZO nanostructure application with good stiffness for long period of usage. The IDE is manufactured utilizing Ag grown on AZO/Si by vacuum coater of thermal evaporator. The I–V measurement has characterized the IDE's electrical properties as a function of frequency and voltage, showing that the current is proportional to voltage. The resistance and capacitance are increased with low frequency and reversely correlated, as force behavior decreases followed by increasing. Alpha-A has been employed to implement another set of measurements. Impedance and capacitance are reversely proportional with frequency and have been affected by voltage. Based on optimum analysis and characterization results, it is concluded that a successful synthesis of AZO nanostructure IDE biosensor device for detection of distinct DNA version was achieved.

Conflicts of interest

The authors declare no conflicts of interest.

Acknowledgments

One of us, K.M.B. is thankful to the Deanship of Scientific Research at King Saud University for its funding through the Research Group Project No. RG-1437-030.

REFERENCES

[1] MacKay S, Hermansen P, Wishart D, Chen J. Simulations of interdigitated electrode interactions with gold nanoparticles for impedance-based biosensing applications. Sensors 2015;15(9):22192–208.
[2] Hanrahan G, Patil DG, Wang J. Electrochemical sensors for environmental monitoring: design, development and applications. J Environ Monit 2004;6(8):657–64.
[3] Radke SM, Alocilja EC. A high density microelectrode array biosensor for detection of E. Coli O157: H7. Biosens Bioelectron 2005;20(8):1662–7.
[4] Guan JG, Miao YQ, Zhang QJ. Impedimetric biosensors. J Biosci Bioeng 2004;97(4):219–26.
[5] Yang L, Li Y, Erf GF. Interdigitated array microelectrode-based electrochemical impedance immunosensor for detection of *Escherichia coli* O157: H7. Anal Chem 2004;76(4):1107–13.
[6] Radke SM, Alocilja EC. Design and fabrication of a micro impedance biosensor for bacterial detection. IEEE Sens J 2004;4:434–40.
[7] Yang L, Li Y. AFM and impedance spectroscopy characterization of the immobilization of antibodies on indium–tin oxide electrode through self-assembled monolayer of epoxysilane and their capture of Escherichia coli O157: H7. Biosens Bioelectron 2005;20(7):1407–16.

[8] Baraket A, Lee M, Zine N, Sigaud M, Bausells J, Errachid A. A fully integrated electrochemical biosensor platform fabrication process for cytokines detection. Biosens Bioelectron 2017;93:170–5.
[9] Zhao W, Xu JJ, Chen HY. Electrochemical biosensors based on layer-by-layer assemblies. Electroanalysis 2006;18(18):1737–48.
[10] Larsen LH, Kjær T, Revsbech NP. A microscale NO3-biosensor for environmental applications. Anal Chem 1997;69(17):3527–31.
[11] Pan Y, Sonn GA, Sin ML, Mach KE, Shih MC, Gau V, et al. Electrochemical immunosensor detection of urinary lactoferrin in clinical samples for urinary tract infection diagnosis. Biosens Bioelectron 2010;26(2):649–54.
[12] Terry LA, White SF, Tigwell LJ. The application of biosensors to fresh produce and the wider food industry. J Agric Food Chem 2005;53(5):1309–16.
[13] Brett AM, Diculescu VC, Chiorcea-Paquim AM, Serrano SH. DNA-electrochemical biosensors for investigating DNA damage. Compr Anal Chem 2007;49:413–37.
[14] Dias CJ, Igreja R. A method of recursive images to obtain the potential, the electric field and capacitance in multi-layer interdigitated electrode (IDE) sensors. Sens Actuators A Phys 2017;256:95–106.
[15] Rana S, Page RH, McNeil CJ. Impedance spectra analysis to characterize interdigitated electrodes as electrochemical sensors. Electrochim Acta 2011;56(24):8559–63.
[16] Brandenburg A, Kita J, Groß A, Moos R. Novel tube-type LTCC transducers with buried heaters and inner interdigitated electrodes as a platform for gas sensing at various high temperatures. Sens Actuators B Chem 2013;189:80–8.
[17] Varshney M, Li Y, Srinivasan B, Tung S. A label-free, microfluidics and interdigitated array microelectrode-based impedance biosensor in combination with nanoparticles immunoseparation for detection of Escherichia coli O157: H7 in food samples. Sens Actuators B Chem 2007;128(1):99–107.
[18] Sanguino P, Monteiro T, Bhattacharyya SR, Dias CJ, Igreja R, Franco R. ZnO nanorods as immobilization layers for interdigitated capacitive immunosensors. Sens Actuators B Chem 2014;204:211–7.
[19] Azizah N, Hashim U, Gopinath SC, Nadzirah S. Gold nanoparticle mediated method for spatially resolved deposition of DNA on nano-gapped interdigitated electrodes, and its application to the detection of the human Papillomavirus. Microchim Ichnoanal Acta 2016;183(12):3119–26.
[20] Siddiquee S, Yusof NA, Salleh AB, Tan SG, Bakar FA. Development of electrochemical DNA biosensor for *Trichoderma harzianum* based on ionic liquid/ZnO nanoparticles/chitosan/gold electrode. J Solid State Electrochem 2012;16(1):273–82.
[21] Haarindraprasad R, Hashim U, Gopinath SC, Perumal V, Liu WW, Balakrishnan SR. Fabrication of interdigitated high-performance zinc oxide nanowire modified electrodes for glucose sensing. Anal Chim Acta 2016;925:70–81.
[22] Molina-Lopez F, Briand D, De Rooij NF. Decreasing the size of printed comb electrodes by the introduction of a dielectric interlayer for capacitive gas sensors on polymeric foil: modeling and fabrication. Sens Actuators B Chem 2013;189:89–96.
[23] Varshney M, Li Y. Interdigitated array microelectrodes based impedance biosensors for detection of bacterial cells. Biosens Bioelectron 2009;24(10):2951–60.
[24] Tang X, Flandre D, Raskin JP, Nizet Y, Moreno-Hagelsieb L, Pampin R, et al. A new interdigitated array microelectrode-oxide-silicon sensor with label-free, high sensitivity and specificity for fast bacteria detection. Sens Actuators B Chem 2011;156(2):578–87.
[25] Yang T, Yu YZ, Zhu LS, Wu X, Wang XH, Zhang J. Fabrication of silver interdigitated electrodes on polyimide films via surface modification and ion-exchange technique and its flexible humidity sensor application. Sens Actuators B Chem 2015;208:327–33.
[26] Tian L, Liu B. Fabrication of CuO nanosheets modified Cu electrode and its excellent electrocatalytic performance towards glucose. Appl Surf Sci 2013;283:947–53.
[27] Preiss EM, Krauss A, Seidel H. Sputtered Pt electrode structures with smoothly tapered edges by bi-layer resist lift-off. Thin Solid Films 2015;597:158–64.
[28] Manzoli A, de Almeida GF, José Filho A, Mattoso LH, Riul A Jr, Mendonca CR, et al. Femtosecond laser ablation of gold interdigitated electrodes for electronic tongues. Opt Laser Technol 2015;69:148–53.
[29] Souiri M, Blel N, Sboui D, Mhamdi L, Epalle T, Mzoughi R, et al. CLSM and EIS characterization of the immobilization of antibodies on indium–tin oxide electrode and their capture of Legionella pneumophila. Talanta 2014;118:224–30.
[30] Sharma D, Lim Y, Lee Y, Shin H. Glucose sensor based on redox-cycling between selectively modified and unmodified combs of carbon interdigitated array nanoelectrodes. Anal Chim Acta 2015;889:194–202.
[31] Ahmad R, Tripathy N, Hahn YB. Wide linear-range detecting high sensitivity cholesterol biosensors based on aspect-ratio controlled ZnO nanorods grown on silver electrodes. Sens Actuators B Chem 2012;169:382–6.
[32] Ren X, Meng X, Chen D, Tang F, Jiao J. Using silver nanoparticle to enhance current response of biosensor. Biosens Bioelectron 2005;21(3):433–7.
[33] Guo H, Tang J, Zhao M, Zhang W, Yang J, Zhang B, et al. Highly stretchable anisotropic structures for flexible micro/nano-electrode applications. Nanoscale Res Lett 2016;11(1):112.
[34] Santangelo S, Patanè S, Frontera P, Pantò F, Triolo C, Stelitano S, et al. Effect of calcium-and/or aluminum-incorporation on morphological, structural and photoluminescence properties of electro-spun zinc oxide fibers. Mater Res Bull 2017;92:9–18.
[35] Norek M, Łuka G, Godlewski M, Płociński T, Michalska-Domańska M, Stępniowski WJ. Plasmonic enhancement of blue emission from ZnO nanorods grown on the anodic aluminum oxide (AAO) template. Appl Phys A 2013;111(1):265–71.
[36] Yun S, Lee J, Chung J, Lim S. Improvement of ZnO nanorod-based dye-sensitized solar cell efficiency by Al-doping. J Phys Chem Solids 2010;71(12):1724–31.
[37] Yang H, Nie S. Preparation and characterization of Co-doped ZnO nanomaterials. Mater Chem Phys 2009;114(1):279–82.
[38] Alkahtani EA, Merad AE, Boufatah MR, Benosman A. DFT investigation of structural, electronic and optical properties of pure and Er-doped ZnO: modified Becke-Johnson exchange potential. Optik 2017;128:274–80.
[39] Dhanalakshmi A, Palanimurugan A, Natarajan B. Enhanced antibacterial effect using carbohydrates biotemplate of ZnO nano thin films. Carbohydr Polym 2017;168:191–200.
[40] Liang CH, Hsiao YJ, Hwang WS. Comparative study of structural and electro-optical properties of ZnO: Ga films grown by steered cathodic arc plasma evaporation and sputtering on plastic and their application on polymer-based organic solar cells. Thin Solid Films 2016;612:419–29.
[41] Dahnoun M, Attaf A, Saidi H, Yahia A, Khelifi C. Structural, optical and electrical properties of zinc oxide thin films deposited by sol-gel spin coating technique. Optik 2017;134:53–9.
[42] Othman AA, Ali MA, Ibrahim EM, Osman MA. Influence of Cu doping on structural, morphological, photoluminescence, and electrical properties of ZnO nanostructures synthesized

by ice-bath assisted sonochemical method. J Alloys Compd 2016;683:399–411.
[43] Gonçalves RS, Barrozo P, Cunha F. Optical and structural properties of ZnO thin films grown by magnetron sputtering: effect of the radio frequency power. Thin Solid Films 2016;616:265–9.
[44] Podbielska H, Ulatowska-Jarża A. Sol-gel technology for biomedical engineering. Bull Polish Acad Sci Tech Sci 2005;53(3):261–71.
[45] Zhongfu X, Gunther P. Silicondioxide electret films prepared by the sol-gel process. IEEE Trans Dielectr Electr Insul 1994;1(1):31–7.
[46] Sakka S. Preparation and properties of sol-gel coating films. J Solgel Sci Technol 1994;2(1–3):451–5.
[47] Srinatha N, Nair KG, Angadi B. Effect of Fe doping on the structural, optical and magnetic properties of combustion synthesized nanocrystalline ZnO particles. Adv Powder Technol 2017;28(3):1086–91.
[48] Rana N, Chand S, Gathania AK. Tailoring the structural and optical properties of ZnO by doping with Cd. Ceram Int 2015;41(9):12032–7.
[49] Raghu P, Srinatha N, Naveen CS, Mahesh HM, Angadi B. Investigation on the effect of Al concentration on the structural, optical and electrical properties of spin coated Al: ZnO thin films. J Alloys Compd 2017;694:68–75.
[50] Shahid MU, Deen KM, Ahmad A, Akram MA, Aslam M, Akhtar W. Formation of Al-doped ZnO thin films on glass by sol–gel process and characterization. Appl Nanosci 2016;6(2):235–41.
[51] Chaitra U, Kekuda D, Rao KM. Effect of annealing temperature on the evolution of structural, microstructural, and optical properties of spin coated ZnO thin films. Ceram Int 2017;43(9):7115–22.
[52] Al-Douri Y, Reshak AH. Analytical investigations of CdS nanostructures for optoelectronic applications. Optik 2015;126(24):5109–14.
[53] Balzaretti NM, Da Jornada JA. Pressure dependence of the refractive index of diamond, cubic silicon carbide and cubic boron nitride. Solid State Commun 1996;99(12):943–8.
[54] Ravindra NM, Auluck S, Srivastava VK. On the Penn gap in semiconductors. Phys Status Solidi B 1979;93(2):K155–60.
[55] Herve PJ, Vandamme LK. Empirical temperature dependence of the refractive index of semiconductors. J Appl Phys 1995;77(10):5476–7.
[56] Ghosh DK, Samanta LK, Bhar GC. A simple model for evaluation of refractive indices of some binary and ternary mixed crystals. Infrared Phys 1984;24(1):43–7.
[57] Al-Douri Y, Khachai H, Khenata R. Chalcogenides-based quantum dots: optical investigation using first-principles calculations. Mater Sci Semicond Process 2015;39:276–82.
[58] Al-Douri Y, Hashim U, Khenata R, Reshak AH, Ameri M, Bouhemadou A, et al. Ab initio method of optical investigations of CdS1− xTex alloys under quantum dots diameter effect. Sol Energy 2015;115:33–9.
[59] Al-Douri Y. Electronic and optical properties of ZnxCd1− xSe. Mater Chem Phys 2003;82(1):49–54.
[60] Al-Douri Y, Feng YP, Huan AC. Optical investigations using ultra-soft pseudopotential calculations of Si0. 5Ge0. 5 alloy. Solid State Commun 2008;148(11–12):521–4.
[61] Al-Douri Y, Reshak AH, Baaziz H, Charifi Z, Khenata R, Ahmad S, et al. An ab initio study of the electronic structure and optical properties of CdS1− xTex alloys. Sol Energy 2010;84(12):1979–84.
[62] Penn DR. Wave-number-dependent dielectric function of semiconductors. Phys Rev 1962;128(5):2093.
[63] Van Vechten JA. Quantum dielectric theory of electronegativity in covalent systems. I. Electronic dielectric constant. Phys Rev 1969;182:891–905.
[64] Samara GA. Temperature and pressure dependences of the dielectric constants of semiconductors. Phys Rev B 1983;27(6):3494.
[65] Lupan O, Pauporté T, Chow L, Viana B, Pellé F, Ono LK, et al. Effects of annealing on properties of ZnO thin films prepared by electrochemical deposition in chloride medium. Appl Surf Sci 2010;256(6):1895–907.
[66] Sharma D, Jha R. Analysis of structural, optical and magnetic properties of Fe/Co co-doped ZnO nanocrystals. Ceram Int 2017;43(11):8488–96.
[67] Lahewil AS, Al-Douri Y, Hashim U, Ahmed NM. Structural and optical investigations of cadmium sulfide nanostructures for optoelectronic applications. Sol Energy 2012;86(11):3234–40.
[68] Lu X, Liu Y, Si X, Shen Y, Yu W, Wang W, et al. Temperature-dependence on the structural, optical, and magnetic properties of Al-doped ZnO nanoparticles. Opt Mater 2016;62:335–40.
[69] Ibraheam AS, Al-Douri Y, Hashim U, Ghezzar MR, Addou A, Ahmed WK. Cadmium effect on optical properties of Cu2Zn1− xCdxSnS4 quinternary alloys nanostructures. Sol Energy 2015;114:39–50.
[70] Gherab K, Al-Douri Y, Voon CH, Hashim U, Ameri M, Bouhemadou A. Aluminium nanoparticles size effect on the optical and structural properties of ZnO nanostructures synthesized by spin-coating technique. Results Phys 2017;7:1190–7.
[71] Xu X, Lin L, Papelis C, Myint M, Cath TY, Xu P. Use of drinking water treatment solids for arsenate removal from desalination concentrate. J Colloid Interface Sci 2015;445:252–61.
[72] Zhong Y, Wang Z, Gao J, Guo Z. A thermodynamic model for agglomeration/defluidization of metal powders based on solid surface energy. Powder Technol 2016;301:1144–7.
[73] Al-Douri Y, Abid H, Aourag H. Correlation between the bulk modulus and the charge density in semiconductors. Physica B Condens Matter 2001;305(2):186–90.
[74] Al-Douri Y, Abid H, Aourag H. Calculation of bulk moduli of semiconductor compounds. Physica B Condens Matter 2002;322(1-2):179–82.
[75] Al-Douri Y. The pressure effect of the bulk modulus seen by the charge density in CdX compounds. Mater Chem Phys 2003;78(3):625–9.
[76] Al-Douri Y, Abid H, Aourag H. Correlation between the bulk modulus and the transition pressure in semiconductors. Mater Lett 2005;59(16):2032–4.
[77] Phillips JC. Bonds and bands in semiconductors. San Diego: Academic Press; 1973.
[78] Harison WA. Electronic structure and the properties of solids. Toronto: General Publishing Company; 1989.
[79] Cohen ML. Calculation of bulk moduli of diamond and zinc-blende solids. Phys Rev B 1985;32(12):7988.
[80] Lam PK, Cohen ML, Martinez G. Analytic relation between bulk moduli and lattice constants. Phys Rev B 1987;35(17):9190.
[81] Al-Douri Y, Abid H, Aourag H. Empirical formula relating the bulk modulus to the lattice constant in tetrahedral semiconductors. Mater Chem Phys 2004;87(1):14–7.